# Carbon single-electron point source controlled by Coulomb blockade

# Carbon single-electron point source controlled by Coulomb blockade

Victor I. Kleshch[1,*], Vitali Porshyn[2], Anton S. Orekhov[3], Andrey S. Orekhov[3,4], Dirk Lützenkirchen-Hecht[2], Alexander N. Obraztsov[1,5]

[1]*Department of Physics, Lomonosov Moscow State University, Moscow 119991, Russia*

[2]*Physics Department, Faculty of Mathematics and Natural Sciences, University of Wuppertal, Wuppertal 42119, Germany*

[3]*Shubnikov Institute of Crystallography of FSRC "Crystallography and Photonics" of the Russian Academy of Sciences, Moscow 119333, Russia*

[4]*Electron Microscopy for Materials Science (EMAT), Department of Physics, University of Antwerp, Antwerp B-2020, Belgium*

[5]*Department of Physics and Mathematics, University of Eastern Finland, Joensuu 80101, Finland*

* Corresponding author, e-mail: klesch@polly.phys.msu.ru

The Coulomb blockade effect is commonly used in solid state electronics for the control of electron flow at the single-particle level. Potentially, it allows the creation of single-electron point sources demanded for prospective electron microscopy instruments and other vacuum electronics devices. Here we realize this potential via creation of a stable point electron source composed of a carbon nanowire electrically coupled to a diamond nanotip by a tunnel junction. Using energy spectroscopy analysis, we characterize the electrons liberated from the nanometer scale carbon heterostructures in time and energy domains. Our experimental results demonstrate perfect agreement with theory prediction of Coulomb oscillations of the Fermi level in the nanowire and allow to determine the mechanisms of their suppression. Persistence of the oscillations at room temperature, high intensity field emission with currents up to 1 μA, and other characteristics of our emitters are very promising for practical realization of coherent single-electron guns.

**Keywords:** carbon nanostructures, nanowires, field emission, Coulomb blockade, single-electron gun

## 1. Introduction

Coulomb blockade is a fundamental phenomenon enabling transfer of individual electrons one by one into electrically isolated nanostructures such as nanowires or quantum dots [1-3] and thereby creation of sources of single electrons [4-6]. Nowadays, solid-state single-electron sources are key elements of the emerging new technologies of quantum information processing and single-electron nanoelectronics [7,8]. Moreover, advanced research in free-electron quantum optics [9] and developments in electron microscopy [10] require the point field emission (FE) cathodes [11-14], which can be controlled at the single electron level [15]. However, up to now, single-electron vacuum guns based on Coulomb blockade were not realized in practice. According to the theoretical predictions, the Coulomb blockade is expected to appear in FE from nanoscale objects weakly coupled to the substrate [16]. It manifests itself in a staircase-like current-voltage characteristic due to single electron charging of the nanoscale emitter. Experimentally, the staircase characteristics were observed for field emitters based on carbon nanotubes [17-19]. In particular, Pascale-Hamri et al. [17] reported well-defined staircases in FE current-voltage curves for a single-wall carbon nanotube tunnel-coupled to a tungsten tip by an amorphous carbon layer. However, the lack of microscopy studies and electron energy spectra measurements did not allow a quantitative comparison with theory. Moreover, as it was shown in [18], the step-like current increase can be attributed not only to the single-electron charging, but also to the resonant tunneling through surface states, which arise due to size quantization. Similar to the case of solid-state devices, these two effects are difficult to separate by means of current-voltage measurements [1]. A reasonable comparison with theory and identification of the actual mechanisms require comprehensive information on morphology of a nanoscale emitter and its electronic structure, which has not been demonstrated experimentally so far. Here we overcome these challenges by creating a field emitter based on a carbon heterostructure composed of a carbon nanowire grown at the diamond nanotip and by determining its electronic and atomic structure using the electron energy spectroscopy and transmission electron microscopy. We unambiguously demonstrate single-electron charging effects by observing directly

Coulomb oscillations of the Fermi level in the carbon nanowire and staircase-like FE current-voltage characteristics. In contrast to the work by Pascale-Hamri et al. [17], we varied the properties of the tunnel barrier between the nanotip and the nanowire within wide limits. This allowed us to reveal that at high FE currents the Coulomb blockade is suppressed either by Joule heating or due to the high tunneling resistance, depending on the nanowire charging time, ranging from about 25 fs to 1 ps. Finally, we perform theoretical simulations of energy spectra and current-voltage characteristics using the theory of FE in Coulomb blockade regime and show excellent agreement between experiment and theory.

## 2. Experimental

**2.1. Samples fabrication.** Heterostructured carbon field emitters were fabricated by a FE-assisted structural modification of diamond needle-like crystals produced by chemical vapor deposition [20]. Here we used the same ultrahigh vacuum (UHV) setup for samples preparation and FE measurements (see next section). However, we note that similar results on FE-assisted fabrication were reproduced using another UHV setup described in ref. [21] as well. First, a diamond needle was fixed on a sharpened tungsten wire, as shown in Fig. 1a, by deposition of a metal (tungsten or platinum) contact, which provided good electrical and mechanical connection [22]. Then, the FE-assisted modification of the diamond surface was performed in the UHV setup. The diamond sample was mounted on the cathode holder and placed at a distance of 0.5 mm from a positively biased mesh gate as shown in Fig. 1b. At a gate voltage of a few hundred volts, the electric field developed at the diamond apex was enough to initiate FE. Conductivity along the needle was provided by defects in the diamond structure concentrated in the pre-surface region [22]. After that, the voltage cycling was performed in order to gradually increase the FE current up to values of 1-10 μA (see Section I of the Supplementary data). As a result of intense Joule heating induced by high current density, the surface layer of the diamond needle with a thickness of a few nanometers was transformed into a-C, which has much higher conductivity. Finally, the growth of a carbon nanowire was initiated on top of the a-C layer by means of a FE-assisted diffusion of surface atoms (see Section III of the Supplementary data). The dimensions of the nanowire and the resistance of

the junction between the nanowire and a-C layer were controlled by changing the parameters of fabrication process.

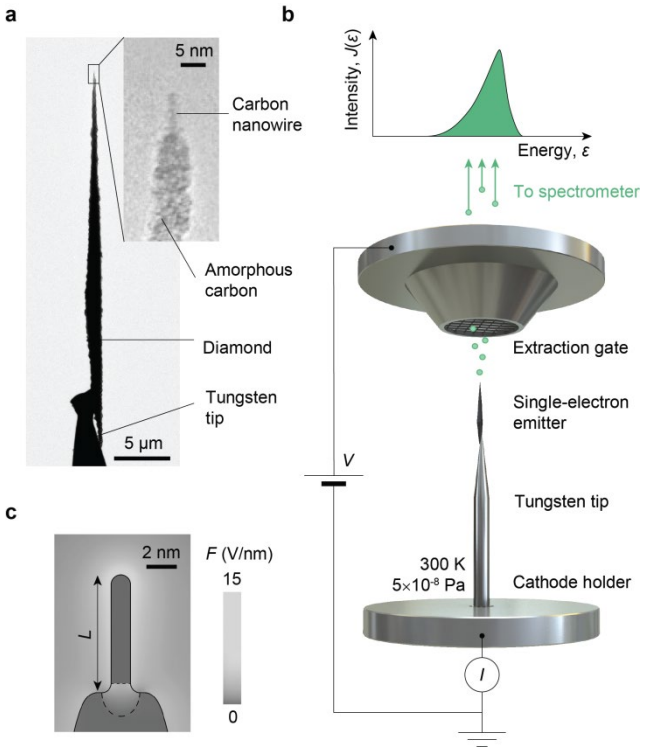


**Fig. 1. Heterostructured carbon field emitter and experimental scheme. (a)** Transmission electron microscopy (TEM) images of a field emitter consisting of a carbon nanowire attached to a diamond needle-like crystal covered by an a-C layer. **(b)** Schematic diagram of the experimental setup. Electrons are field emitted one by one from a single-electron source under a DC voltage, $V$, applied to the mesh gate electrode. The total energy distribution of the emitted electrons, $J(\varepsilon)$, is measured using a hemispherical spectrometer. The FE current, $I$, is measured by a picoammeter connected to the cathode. **(c)** Simulated distribution of the electric field strength, $F$, for the emitter shown in (a) at a gate voltage $V = 80$ V (see Section V of the Supplementary data). $L$ is the length of the nanowire. The dashed lines mark the boundaries of a depletion zone, formed at the junction of the nanowire and the a-C layer. Single-electron effects in FE from the nanowire are possible due to the formation of a double-barrier structure with a Schottky-type barrier in the depletion zone and a FE-barrier at the nanowire/vacuum interface.

**2.2. FE measurements.** The FE measurements were performed at $5\times10^{-8}$ Pa pressure and at room temperature using an UHV setup (Fig. 1b) described in more detail in ref. [23]. The strong field at the nanowire apex was created by a positively biased mesh gate. The electrons emitted from the nanowire were transmitted through the gate and collected by a hemispherical analyzer. The total current, $I$, and the

total electron energy distribution, $J(\varepsilon)$, were measured as a function of the gate voltage, $V$. A positive DC voltage was applied to the gate electrode using a high voltage power supply (FuG HCN 35-35000) and was measured with a multimeter (Solartron 7150plus). The FE current was measured by a picoammeter (Keithley 6485) connected to the cathode electrode. Current-voltage characteristics were obtained by ramping the voltage and registering the current with a time interval of 0.2-1 s between the measurements. Total energy distributions were measured using a spectrometer (SPECS Phoibos 100) with a hemispherical analyzer. The maps of total energy distributions were obtained by measuring a series of spectra at various voltages, with a rate and integration time of about 5 s and 1 s, respectively. The intensity of each spectrum was normalized to unity for each voltage value (see details in Section II of the Supplementary data).

## 3. Results and discussion

**3.1. FE current measurements.** A typical FE electron source (cathode) under study is shown in Fig. 1a. It was fabricated by a FE-assisted structural modification of a micrometer-scale needle-like diamond crystal as described in Experimental section. It consists of a carbon nanowire extending from an amorphous carbon (a-C) layer which covers the diamond surface. Figure 2a shows a typical current-voltage, $I(V)$, dependence for one of the investigated carbon nanowire emitters. The most remarkable feature is a clear staircase-like pattern, which was observed in the $I(V)$ curves plotted in semi-logarithmic coordinates. The variations in FE are more evident from the dependence of the normalized differential conductance, $(\mathrm{d}I/\mathrm{d}V)/(I/V)$, on the applied voltage, demonstrating oscillations with a constant period, $\Delta V$. Similar staircase $I(V)$ behavior was reproducibly obtained for more than 10 samples with $\Delta V$ varying from 8 to 250 V, depending on the fabrication conditions. Moreover, by means of a high-current processing, it was possible to gradually shorten (or lengthen) the carbon nanowire and, correspondingly, increase (or decrease) $\Delta V$ in a certain range (see Section I of the Supplementary data). An example of such modification is presented in Fig. 2b, which shows the results of three subsequent measurements demonstrating $\Delta V$ decrease with an increase in the nanowire length, $L$.

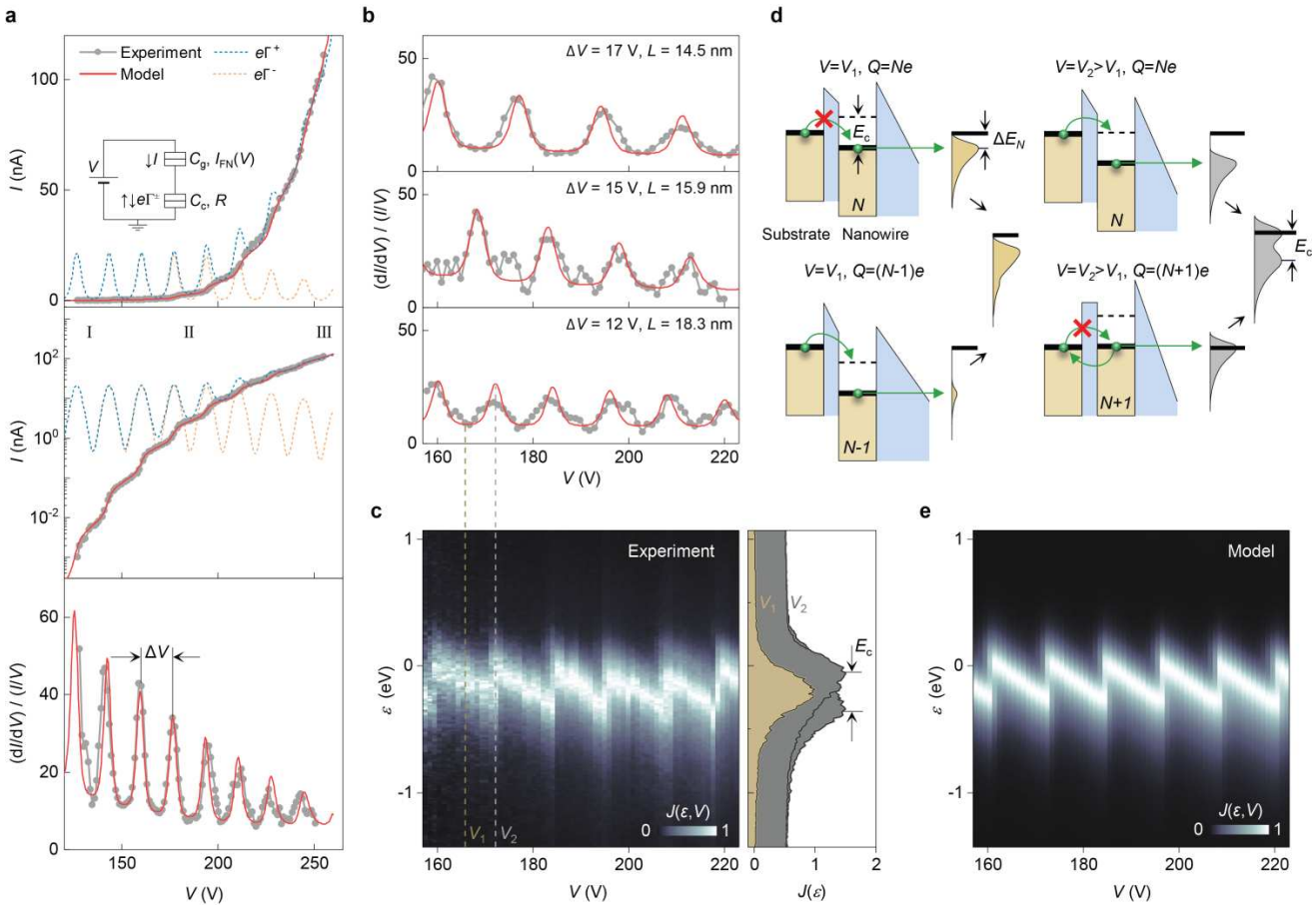


**Fig. 2. Coulomb oscillations in FE from a carbon nanowire**. **(a)** Experimental and simulated staircase-like current-voltage characteristics, $I(V)$, in linear (upper panel) and semi-logarithmic (middle panel) coordinates, and the corresponding oscillations of the normalized differential conductivity (upper panel), $(\mathrm{d}I/\mathrm{d}V)/(I/V)$, with a period of $\Delta V$. The dashed lines are the dependences of $e\Gamma^{\pm}$ on $V$, where $e$ is the elementary charge and $\Gamma^{\pm}$ are the simulated average tunneling rates in the junction between the nanowire and the substrate. The inset shows an equivalent circuit of a double-barrier system consisting of a tunnel barrier between the nanowire and the substrate with resistance $R$ and a FE-barrier, which exhibits a Fowler-Nordheim-type (FN-type) current-voltage characteristic, $I_{\mathrm{FN}}(V)$. $C_{\mathrm{c}}$ and $C_{\mathrm{g}}$ are the capacitances of the nanowire with respect to the rest of the cathode and to the gate, respectively. **(b)** Three subsequent measurements (gray circles) of the differential conductivity with different periods, $\Delta V$, and their fits (red curves). The decrease in $\Delta V$ is associated with the increase in the nanowire length, $L$, due to the growth process, which was performed between the measurements. **(c)** Sawtooth-like oscillations in the normalized total energy distribution map, $J(\varepsilon, V)$, measured together with the differential conductivity presented in the lower panel of (b). The dashed lines show voltages $V_1$ and $V_2$ at which the cross-sections (right panel) are made. **(d)** Energy diagrams of the double-barrier system at two voltages $V_{1,2}$ defined in (c) and different charges, $Q$, of the nanowire (see main text). **(e)** Simulated total energy distribution map corresponding to the experimental data in (c).

**3.2. Coulomb oscillations in FE spectra.** As we pointed out above, the staircase-like increase of FE current was previously observed in particular conditions for carbon nanotubes [17-19], while this is not typical for FE phenomenon in general. However, the most striking result obtained in our experiments is the dependence of electron energy spectra on the gate voltage. Figure 2c presents the normalized total energy distributions visualized in a two-dimensional map, $J(\varepsilon, V)$, where $\varepsilon$ is the kinetic electron energy relative to the Fermi level of the cathode electrode. In the region between two maxima of the differential conductance, the spectrum consists of a single peak, as demonstrated by the map cross-section at $V_1$. The peak shifts downward in energy with increasing voltage until the maximum of the differential conductance is reached at $V_2$. Here, another peak appears at $\varepsilon$=0 eV and continues to shift with increasing voltage, while the lower-energy peak disappears. Thus, the peak position oscillates with the gate voltage and follows a remarkable "sawtooth-like" dependence with a period $\Delta V$.

The double-peak spectrum at $V_2$ indicates the presence of two different energy states, which could be associated with quantum confinement. However, confined field emitters, e.g. adsorbed atoms [24] or nanoscale metal protrusions [25], usually exhibit a continuous shift of discrete energy peaks with the applied voltage (because of the field penetration effect), rather than periodic oscillations. The principal novelty of our FE structure is that the nanowire is electrically isolated from the a-C layer by a potential barrier (Fig. 1c) formed due to the difference in concentrations of $sp^2$-bonded carbon atoms (see Section III of the Supplementary data). As a result, a double-barrier structure arises and the Coulomb blockade effect becomes possible, since the addition of an extra electron to the nanowire, having a very low capacitance, requires a considerable energy $E_c$ (charging energy). Thus, in this case, FE is affected by the quantization of charge, rather than the size quantization, which is negligible compared to the Coulomb interaction in our carbon nanowires.

**3.3. Electron transport model.** The energy diagram explaining transport in the double-barrier structure is presented in Fig. 2d. The nanowire is isolated by a tunnel barrier from the substrate, which has a fixed Fermi level. At voltage $V_1$ the nanowire appears mainly in two states with $N$ and $N$-1 electrons.

In the $N$-electron state the transfer of an electron from the substrate to the nanowire is energetically unfavorable, since with the addition of an electron the nanowire Fermi level increases by $E_c$ and, thus, exceeds the substrate Fermi level. Therefore, the nanowire remains in the $N$-electron state until an electron tunnels into vacuum. In the ($N$-1)-electron state, electron tunneling into vacuum is much less probable than the substrate-nanowire tunneling. As a result, at $V=V_1$, FE predominantly occurs from the $N$-electron state and the spectrum consists of a single peak shifted relative to the substrate Fermi level by $\Delta E_N$, which is the Coulomb energy difference for the nanowire with $N$ and $N$-1 electrons. The nanowire Fermi level defined by $\Delta E_N$ shifts downward with the voltage increase. At $V=V_2$ it aligns with the cathode Fermi level ($\Delta E_N=E_c$) and the transition to the ($N$+1)-electron state becomes favorable. In this case, FE occurs from both states with $N$ and $N$+1 electrons and, correspondingly, two peaks separated by $E_c$ are observed in the energy spectrum.

The modeling of the current-voltage characteristics for the described double-barrier system was performed using the theory of FE in the Coulomb blockade regime, which was first proposed in ref. [16]. Moreover, here we extend this theory to model the electron energy spectra, taking into account the voltage drop inside the emitter and Joule heating.

The FE current and electron energy spectra are determined by the probabilities, $P_N$, to find the nanowire in a state with $N$ electrons at a given voltage, $V$. According to the conventional Coulomb-blockade theory, $P_N$ can be found by solving the master equation [3], which in steady state can be written using detailed balance condition and has the following form

$$e\Gamma_N^- P_N + I_N P_N = e\Gamma_N^+ P_{N-1}. \qquad (1)$$

Here the left side corresponds to the departure of an electron from the nanowire in the $N$-electron state and contains partial FE current, $I_N$, and tunneling rate from the nanowire to the substrate, $\Gamma_N^-$. Since no electrons arrive from the gate, the right side does not contain the FE term and depends only on the tunneling rate from the substrate to nanowire $\Gamma_N^+$, which describes the arrival of an electron at the nanowire in an ($N$-1)-electron state. Tunneling rates are given by [3]

$$\Gamma_N^- = \frac{\Delta E_N}{e^2 R} \frac{1}{1 - \exp(-\Delta E_N / k_B T)},$$
$$\Gamma_N^+ = \Gamma_N^- \exp(-\Delta E_N / k_B T), \quad (2)$$

where $R$ is substrate-nanowire junction resistance, and $\Delta E_N$ is the difference in the Coulomb energies of the system for a nanowire with $N$ and $N$-1 electrons. For the equivalent circuit of the system (inset of Fig. 2a) it is given by [16]

$$\Delta E_N = E_c(N - 1/2 - C_g V/e), \quad (3)$$

where $E_c = e^2/C$ is the charging energy, $C = C_c + C_g$ is the total capacitance, $C_g$ and $C_c$ are the capacitances of the nanowire with respect to the gate and to the rest of the cathode, respectively.

The partial FE currents, $I_N$, are given by the modified Fowler-Nordheim equation, which takes into account the high curvature of the carbon nanowire [26]

$$I_N = A F_N^2 \exp(-B/F_N - C/F_N^2), \quad (4)$$

where $A$, $B$, $C$ are the parameters determined by fitting the experimental $I(V)$ curve, and $F_N$ is the field strength at the nanowire apex in the state with $N$ electrons (see Section IV of the Supplementary data). The values of $F_N$ were determined by the numerical finite-element simulation of electric field distribution in the system, as described in Section V of the Supplementary data. An example of such a calculation is shown in Fig. 1c. It should be noted that, the Coulomb oscillation period is determined by $\Delta V = e/C_g$, as follows from the equation (3). $C_g$ and $C_c$ are determined by the geometry of the system and, in particular, by the length, $L$, and diameter, $D$, of the nanowire, which were varied during the finite-element simulations to match the capacitances. In particular, the values of $L$ at different $\Delta V$, shown in Fig. 2b, were obtained using this procedure.

By substituting expressions (2-4) into equation (1), we obtain the system of equations, which solution gives the probabilities $P_N$. Then, the total FE current and average tunneling rates can be calculated as the sum over all states as

$$I = \sum_N I_N P_N,$$

$$\Gamma^{\pm} = \sum_N \Gamma_N^{\pm} P_N.$$

Similarly, the energy spectrum is calculated as a sum over all spectra corresponding to each *N*-electron state as

$$J(\varepsilon) = \sum_N j(\varepsilon - \Delta E_N) P_N, \qquad (6)$$

where $j(\varepsilon)$ is the total energy distribution shifted in energy from the cathode Fermi level ($\varepsilon = 0$) by $\Delta E_N$ (Fig. 2d). The dependence $j(\varepsilon)$ is given by the FE theory [27] and takes into account the high curvature of the carbon nanowire [28] (see Section IV of the Supplementary data). By using equations (5) and (6), we fitted the experimental data and obtained the model parameters. The values of the parameters used for the simulations in Figs. 2-4 are given in the Section V of the Supplementary data.

**3.4. Simulation results.** Obtained experimental data are well reproduced by the presented model Figure 2 shows the simulated spectra and fits of $I(V)$ curves, from which we obtained the model parameters, including the dimensions of the nanowire, substrate-nanowire junction resistance, $R$, and the nanowire total capacitance, $C$. It should be noted that the curves in Fig. 2b, are perfectly fitted using the same set of parameters with the only variable being the nanowire length, $L$. This is clear evidence that the changes in the oscillation period $\Delta V$ in the experiment can be associated with the variation of $L$. It is also important to note that the fitting results coincide with the results of electrostatic simulations of a nanowire, based on its dimensions estimated from TEM images. In particular, the simulated nanowire-gate capacitance, $C_g$, obtained from the electric field distribution (Fig. 1c), coincides well with the analytical formula $C_g = e/\Delta V$ given by the model (see Section V of the Supplementary data). This good agreement validates the assumption that the nanowire is isolated from the substrate.

To elucidate the mechanism of Coulomb oscillations, we calculated the average tunneling rates between the substrate and nanowire, $\Gamma^{\pm}$, which are related to the FE current as $I = e(\Gamma^{+} - \Gamma^{-})$.

$\Gamma^{\pm}(V)$ dependences are shown in Fig. 2a, where three voltage regions can be distinguished. At low voltages (Region I), both $e\Gamma^{\pm}$ significantly exceed the FE current. At intermediate voltages (Region II), the FE barrier becomes more transparent and the substrate–nanowire tunneling rate $\Gamma^{+}$ increases with $I$, while the reverse tunneling rate $\Gamma^{-}$ remains approximately unchanged. At high voltages (Region III), Coulomb oscillations are gradually suppressed and $I \approx e\Gamma^{+}$, while $\Gamma^{-}$ decreases. A similar behavior of $\Gamma^{\pm}(V)$ was observed for all samples, however, the absolute values of $\Gamma^{\pm}$ varied significantly. $\Gamma^{\pm}$ can be estimated roughly by the reciprocal of the charging time constant $\Gamma^{\pm} \sim (RC)^{-1}$. For different samples we obtained $RC$ in the range from 25 fs to 1.5 ps. In the following, we consider two representative cases of the highest and lowest $RC$ values, shown in Fig. 3 and Fig. 4, respectively.

**3.5. Coulomb blockade suppression mechanisms.** Figure 3 presents the results for the sample with a large $RC$ of 1.5 ps, which results from a high $R$ value of 3 MΩ. This sample was obtained at a lower current than the sample considered in Fig. 2 and, therefore, had a higher tunneling resistance $R$ and a higher resistance of the support needle $R_0$ (see Section III of the Supplementary data). In this case an overall shift of the spectrum with voltage (Fig. 3a) was observed, as a result of an additional voltage drop, $IR_0$, inside the poorly conductive diamond needle with $R_0 \sim 90$ MΩ. More importantly, the energy peaks which correspond to the states with different numbers of electrons were found to coexist in a certain voltage region, see e.g. $N$+4 and $N$+5 states in Fig. 3b. Here, the tunneling rates through both barriers become comparable, i.e. $RC \sim e/I$, where $e/I$ is the average time between subsequent FE events. The number of coexisting electron levels increases with FE current, and the Coulomb oscillations become completely suppressed for $RC \gg e/I$. This is demonstrated in Fig. 3c, where we also present two other characteristic time intervals: the uncertainty time, $\tau_q$, and tunneling time, $\tau_t$. The Coulomb-blockade theory [3] claims that $RC \gg \tau_q \gg \tau_t$, is a necessary condition for the observation of single-electron charging effects. The above analysis shows that for the system with a FE barrier an additional condition $e/I \gg RC$ must hold as well.

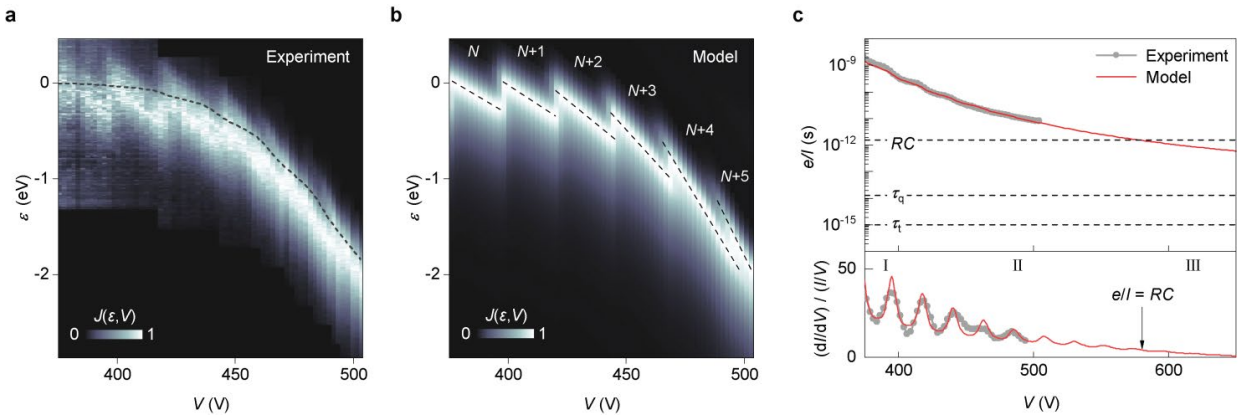


**Fig. 3. Coulomb oscillations for a large-*RC* field emitter. (a)** Experimental total energy distribution map. The dashed line is the electron energy loss, $eIR_0$, associated with the voltage drop inside the diamond needle with a resistance $R_0$. **(b)** Simulated total energy distribution map obtained at $RC$ = 1.5 ps. The dashed lines are the positions of energy peaks corresponding to the states with a different number of electrons. **(c)** The average time between electron FE events, $e/I(V)$, and the corresponding normalized differential conductivity, $(\mathrm{d}I/\mathrm{d}V)/(I/V)$. The fits (red lines) are obtained using the same parameters as in (b). The dashed lines represent the $RC$-time constant, the uncertainty time $\tau_q$ and the tunneling time $\tau_t$. The uncertainty time equals $\tau_q = R_qC$, where $R_q = h/e^2 \sim 25.8$ kΩ is the quantum unit of resistance. It is associated with the time-energy uncertainty relation $E_c\tau_q \sim h$, with a charging energy $E_c = e^2/C$. The tunneling time, $\tau_t$, is the time spent by tunneling electron under the barrier. It is generally assumed to be of about $10^{-15}$ s.

The most important feature for emitters with small $RC$ values is the strong broadening of the spectra with the applied voltage, as demonstrated in Fig. 4a for a sample with $RC$=25 fs. Performed modeling shows that the broadening is associated with an increase in the emitter temperature, $T$, due to Joule heating (see Section VI of the Supplementary data). The $T(V)$ dependence was directly extracted from the fits of the spectra and it was found that the oscillations almost completely disappear at $T>T_C$=850 K (Fig. 4c). Thus, unlike the large-$RC$ case, here the single-electron effects are suppressed due to an increase in the thermal fluctuation energy, $k_BT$, which becomes comparable with the charging energy $E_c$, namely $E_c \sim 10k_BT_C$, in agreement with the Coulomb-blockade theory [3]. The critical temperature $T_C$ is reached at $I$ of about 1 μA and, correspondingly, $e/I$ is of about 0.2 ps, indicating that the FE-barrier effective tunneling rate is of about 5 THz. It is also worth noting that oscillation period

here reaches 250 V. These remarkable characteristics, that are difficult to observe by employing conventional Coulomb-blockade-controlled solid-state devices, are achieved here due to the special geometry of the system (the drain is at a macroscopic distance from the source) and a small size of the nanowire with the high charging energy and short *RC* time.

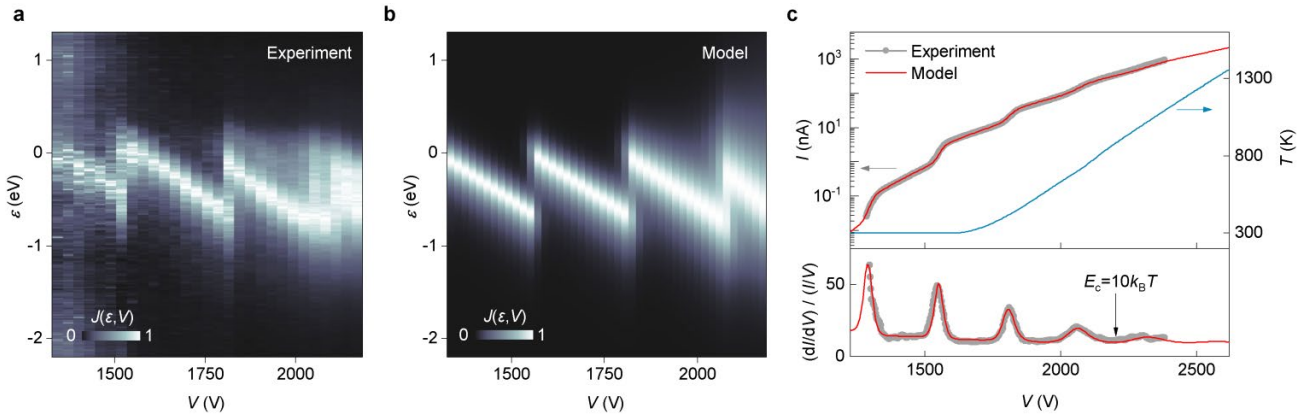


**Fig. 4. Coulomb oscillations for a small-*RC* field emitter. (a)** Experimental total energy distribution map, showing the broadening of the spectra with increasing voltage. **(b)** Simulated total energy distribution map obtained at $RC = 0.025$ ps using $T(V)$ dependence. **(c)** Current-voltage curve, $I(V)$, and the corresponding normalized differential conductivity, $(\mathrm{d}I/\mathrm{d}V) / (I/V)$. The blue curve is the emitter temperature dependence, $T(V)$, obtained by fitting the experimental spectra (see Section VI of the Supplementary data). The fits (red lines) are obtained using the same parameters as in (b).

## 4. Conclusions

To summarize, we report on the Coulomb blockade in an all-carbon heterostructured field emitter. Due to the strong carbon–carbon bonding, stable Coulomb oscillations persist at large currents, high tunneling frequencies and above room temperature. The small emission area and one-by-one electron tunneling make the liberated electrons more coherent both in space [29] and in time [30], in comparison with conventional metal-tip field emitters. These characteristics may be very attractive for practical implementation of coherent single-electron guns. We anticipate that the combination of introduced carbon single-electron sources with laser-induced gating [31] is highly promising for the creation of coherent ultrashort free-electron bunches of interest for low-energy electron holography [32,33] and

ultrafast electron or X-ray imaging and spectroscopy [34,35]. Moreover, the total energy distribution maps presented here provide direct access to states probability distributions, temperature and other parameters, and therefore can be considered as a new method of single-electron spectroscopy, alternative to measurements of capacitance [36] and conductivity [37], which are used in solid-state systems. Finally, thanks to the high charging energy and nanometer size, heterostructured carbon tips can be used to probe local electrostatic potential fields with nanometer resolution, similar to the recently developed scanning quantum dot microscopy [38,39].

**Acknowledgements**

The work was supported by Russian Science Foundation (Project No. 19-72-10067).

**References**

[1] B. Su, V. J. Goldman, and J. E. Cunningham, *Observation of single-electron charging in double-barrier heterostructures*, Science **255**, 313 (1992).

[2] M. H. Devoret, D. Esteve, and C. Urbina, *Single-electron transfer in metallic nanostructures*, Nature **360**, 547 (1992).

[3] K. K. Likharev, *Single-electron devices and their applications*, Proc. IEEE **87**, 606 (1999).

[4] G. Feve, A. Mahe, J. M. Berroir, T. Kontos, B. Placais, D. C. Glattli, A. Cavanna, B. Etienne, and Y. Jin, *An on-demand coherent single-electron source*, Science **316**, 1169 (2007).

[5] R. Hanson, L. P. Kouwenhoven, J. R. Petta, S. Tarucha, and L. M. K. Vandersypen, *Spins in few-electron quantum dots*, Rev. Mod. Phys. **79**, 1217 (2007).

[6] M. Brotons-Gisbert, A. Branny, S. Kumar, R. Picard, R. Proux, M. Gray, K. S. Burch, K. Watanabe, T. Taniguchi, and B. D. Gerardot, *Coulomb blockade in an atomically thin quantum dot coupled to a tunable Fermi reservoir*, Nat. Nanotechnol. **14**, 442 (2019).

[7] C. Bauerle, D. C. Glattli, T. Meunier, F. Portier, P. Roche, P. Roulleau, S. Takada, and X. Waintal, *Coherent control of single electrons: a review of current progress*, Rep. Prog. Phys. **81**, 056503, 056503 (2018).

[8] K. Tapio, J. Leppiniemi, B. X. Shen, V. P. Hytonen, W. Fritzsche, and J. J. Toppari, *Toward single electron nanoelectronics using self-assembled DNA structure*, Nano Lett. **16**, 6780 (2016).

[9] H. Kiesel, A. Renz, and F. Hasselbach, *Observation of Hanbury Brown-Twiss anticorrelations for free electrons*, Nature **418**, 392 (2002).

[10] A. H. Zewail, *Four-dimensional electron microscopy*, Science **328**, 187 (2010).

[11] H. Zhang, J. Tang, J. S. Yuan, Y. Yamauchi, T. T. Suzuki, N. Shinya, K. Nakajima, and L. C. Qin, *An ultrabright and monochromatic electron point source made of a LaB6 nanowire*, Nat. Nanotechnol. **11**, 273 (2016).

[12] X. S. Yuan, Y. Zhang, M. T. Cole, Y. Yan, X. Y. Li, R. Parmee, J. Q. Wu, N. S. Xu, W. I. Milne, and S. Z. Deng, *A truncated-cone carbon nanotube cold-cathode electron gun*, Carbon **120**, 374 (2017).

[13] X. Y. Shao, A. Srinivasan, W. K. Ang, and A. Khursheed, *A high-brightness large-diameter graphene coated point cathode field emission electron source*, Nat. Commun. **9**, 1288, 1288 (2018).

[14] M. Lorenzo, C. Escher, T. Latychevskaia, and H. W. Fink, *Metal Adsorption and Nucleation on Free-Standing Graphene by Low-Energy Electron Point Source Microscopy*, Nano Lett. **18**, 3421 (2018).

[15] T. Esat, N. Friedrich, F. S. Tautz, and R. Temirov, *A standing molecule as a single-electron field emitter*, Nature **558**, 573 (2018).

[16] O. E. Raichev, *Coulomb blockade of field emission from nanoscale conductors*, Phys. Rev. B **73**, 195328, 195328 (2006).

[17] A. Pascale-Hamri, S. Perisanu, A. Derouet, C. Journet, P. Vincent, A. Ayari, and S. T. Purcell, *Ultrashort single-wall carbon nanotubes reveal field-emission Coulomb blockade and highest electron-source brightness*, Phys. Rev. Lett. **112**, 126805, 126805 (2014).

[18] S. M. Lyth and S. R. P. Silva, *Resonant behavior observed in electron field emission from acid functionalized multiwall carbon nanotubes*, Appl. Phys. Lett. **94**, 123102, 123102 (2009).

[19] V. I. Kleshch, V. A. Eremina, P. Serbun, A. S. Orekhov, D. Lutzenkirchen-Hecht, E. D. Obraztsova, and A. N. Obraztsov, *A comparative study of field emission from semiconducting and metallic single-walled carbon nanotube planar emitters*, Phys. Status Solidi B **255**, 1700268, 1700268 (2018).

[20] A. N. Obraztsov, P. G. Kopylov, B. A. Loginov, M. A. Dolganov, R. R. Ismagilov, and N. V. Savenko, *Single crystal diamond tips for scanning probe microscopy*, Rev. Sci. Instrum. **81**, 013703, 013703 (2010).

[21] D. Lysehkov and G. Muller, *Field emission measurement techniques for the optimisation of carbon nanotube cathodes*, Int. J. Nanotechnol. **2**, 239 (2005).

[22] V. I. Kleshch, S. T. Purcell, and A. N. Obraztsov, *Single crystal diamond needle as point electron source*, Sci. Rep. **6**, 35260, 35260 (2016).

[23] S. Mingels, V. Porshyn, B. Bornmann, D. Lutzenkirchen-Hecht, and G. Muller, *Sensitive fast electron spectrometer in adjustable triode configuration with pulsed tunable laser for research on photo-induced field emission cathodes*, Rev. Sci. Instrum. **86**, 043307, 043307 (2015).

[24] E. W. Plummer and R. D. Young, *Field-emission studies of electronic energy levels of adsorbed atoms*, Phys. Rev. B **1**, 2088 (1970).

[25] V. T. Binh, S. T. Purcell, N. Garcia, and J. Doglioni, *Field-emission electron-spectroscopy of single-atom tips*, Phys. Rev. Lett. **69**, 2527 (1992).

[26] J. He, P. H. Cutler, and N. M. Miskovsky, *Generalization of Fowler-Nordheim field-emission theory for nonplanar metal emitters*, Appl. Phys. Lett. **59**, 1644 (1991).

[27] R. D. Young, *Theoretical total-energy distribution of field-emitted electrons*, Phys. Rev. **113**, 110 (1959).

[28] G. N. Fursey and D. V. Glazanov, *Deviations from the Fowler-Nordheim theory and peculiarities of field electron emission from small-scale objects*, J. Vac. Sci. Technol. B **16**, 910 (1998).

[29] H. Schmid and H. W. Fink, *Carbon nanotubes are coherent electron sources*, Appl. Phys. Lett. **70**, 2679 (1997).

[30] A. Mahe, F. D. Parmentier, E. Bocquillon, J. M. Berroir, D. C. Glattli, T. Kontos, B. Placais, G. Feve, A. Cavanna, and Y. Jin, *Current correlations of an on-demand single-electron emitter*, Phys. Rev. B **82**, 201309, 201309 (2010).

[31] M. Kozak, J. McNeur, K. J. Leedle, H. Deng, N. Schonenberger, A. Ruehl, I. Hartl, J. S. Harris, R. L. Byer, and P. Hommelhoff, *Optical gating and streaking of free electrons with sub-optical cycle precision*, Nat. Commun. **8**, 14342, 14342 (2017).

[32] J. N. Longchamp, S. Rauschenbach, S. Abb, C. Escher, T. Latychevskaia, K. Kern, and H. W. Fink, *Imaging proteins at the single-molecule level*, Proc. Natl. Acad. Sci. U.S.A. **114**, 1474 (2017).

[33] L. Vicarelli, V. Migunov, S. K. Malladi, H. W. Zandbergen, and R. E. Dunin-Borkowski, *Single electron precision in the measurement of charge distributions on electrically biased graphene nanotips using electron holography*, Nano Lett. **19**, 4091 (2019).

[34] H. W. Kim, N. A. Vinokurov, I. H. Baek, K. Y. Oang, M. H. Kim, Y. C. Kim, K. H. Jang, K. Lee, S. H. Park, S. Park, J. Shin, J. Kim, F. Rotermund, S. Cho, T. Feurer, and Y. U. Jeong, *Towards jitter-free ultrafast electron diffraction technology*, Nat. Photonics **14**, 245 (2020).

[35] K. E. Priebe, C. Rathje, S. V. Yalunin, T. Hohage, A. Feist, S. Schaer, and C. Ropers, *Attosecond electron pulse trains and quantum state reconstruction in ultrafast transmission electron microscopy*, Nat. Photonics **11**, 793 (2017).

[36] R. C. Ashoori, H. L. Stormer, J. S. Weiner, L. N. Pfeiffer, S. J. Pearton, K. W. Baldwin, and K. W. West, *Single-electron capacitance spectroscopy of discrete quantum levels*, Phys. Rev. Lett. **68**, 3088 (1992).

[37] P. L. McEuen, E. B. Foxman, U. Meirav, M. A. Kastner, Y. Meir, N. S. Wingreen, and S. J. Wind, *Transport spectroscopy of a Coulomb island in the quantum Hall regime*, Phys. Rev. Lett. **66**, 1926 (1991).

[38] C. Wagner, M. F. B. Green, P. Leinen, T. Deilmann, P. Kruger, M. Rohlfing, R. Temirov, and F. S. Tautz, *Scanning quantum dot microscopy*, Phys. Rev. Lett. **115**, 026101, 026101 (2015).

[39] C. Wagner, M. F. B. Green, M. Maiworm, P. Leinen, T. Esat, N. Ferri, N. Friedrich, R. Findeisen, A. Tkatchenko, R. Temirov, and F. S. Tautz, *Quantitative imaging of electric surface potentials with single-atom sensitivity*, Nat. Mater. **18**, 853 (2019).